

# Metasurface Approach to Generate Homogeneous $B_1^+$ Field for High-Field and Ultra-High-Field MRI

Chen Xue , Guanglei Zhou , and Alex M. H. Wong , *Senior Member, IEEE*

**Abstract**—A novel electromagnetic excitation method – the Huygens’ cylinder – is proposed to improve the  $B_1^+$  field homogeneity of the high-field (HF) and ultra-high field (UHF) magnetic resonance imaging (MRI). Based on the concept of the Huygens’ box, we calculate the currents on a cylindrical boundary that can synthesize an arbitrary electromagnetic wave inside the enclosed region. Specifically, we excite a right-handed circularly polarized ( $B_1^+$ ) travelling wave with high mode purity inside the Huygens’ cylinder coil. The simulated  $B_1^+$  field obtained from several 3T and 7T MR scenarios are reported and compared with birdcage coils. In the unloaded scenarios, the Huygens’ cylinder achieves superior  $B_1^+$ -field homogeneity over both the sagittal and axial plane compared to the birdcage coil for both 3T and 7T MRI. In the loaded scenarios, the Huygens’ cylinder achieves superior  $B_1^+$ -field homogeneity over the sagittal plane and comparable  $B_1^+$ -field homogeneity over the axial plane for both 3T and 7T MRI compared to the birdcage coil. Moreover, the 7T Huygens’ cylinder can generate a uniform field over a much larger region, enabling the imaging of a large part of the human body. The Huygens’ cylinder greatly improves the homogeneity of  $B_1^+$  field and is free from the dielectric resonance limitation suffered by conventional RF coils. It has strong potential as future RF coils in HF and UHF MR systems.

**Index Terms**—Electromagnetic field homogeneity, metamaterial, metasurface, ultra-high field MRI.

## I. INTRODUCTION

HF AND UHF MRI has gained immense recent interest because the resolution of the MR image improves vastly with an increased static magnetic field. However, in these high-field systems, the problem of  $B_1^+$  field inhomogeneity becomes a major hurdle. An inhomogeneous RF field illuminates the patient unevenly and creates unilluminated areas, “bright spots” and “dark spots” which degrade the resultant MR image [1].

At low-field MRI (1.5T), conventional designs like the birdcage coil have been demonstrated to produce a highly homogeneous field for clinical use [2]. However, this method is based upon an electrostatic approximation [2], [3], which fails to apply

as the Larmor frequency increases with the static field strength. When the working frequency increases, the wavelength correspondingly decreases to render inapplicable the electrostatic approximation. The effective wavelength further decreases when the patient (human or animal) is inside the cavity because their body tissues often have high dielectric constants. This worsens the RF field inhomogeneity in 3T and 7T systems.

The shortening of the effective wavelength makes it difficult to design wide-bore large-sized RF coils. The RF field homogeneity worsens with increasing MRI field strength and frequency due to the dielectric resonance effect [4]. To combat problems related to field-homogeneity at high field strengths, researchers have developed the multiple-resonance birdcage coil [5]. However, this method has an obvious drawback of having significant RF losses, which limits its usage for UHF MRI (>7T). Moreover, the multiple-resonance birdcage can only be applied on small-sized coils, because the homogeneity will decay quickly when its size increases. As a result, it is mainly applied in imaging small test subjects such as the head of mice [6]. Besides multiple-resonance birdcage coils, various structure-modified birdcage coils, like spiral birdcage coils [7], high-pass birdcage coils with endcaps [8] and birdcage coil arrays [9] are developed. Although they improve the field uniformity slightly, they cannot solve the problem fundamentally. In addition to the modified birdcage coils, dipole antenna arrays [10] are also used to improve the uniformity, while it is limited by the electrical length. Microstrip coils [11] can reduce the dependence on electrical length, but the performance is highly dependent on the width and length of the microstrip, and it doesn’t work well at low frequency.

Beyond the conventional RF coils, other electromagnetic structures with homogeneous magnetic fields have also been investigated with interest. The travelling-wave (TW) MRI [12] has been proposed, where the MRI bore is used as a circular waveguide. Using two circularly polarized patch antennas at two ends of the MRI bore, a circularly polarized travelling wave, which has reasonable field homogeneity, can be launched inside the bore. However, as the frequency increases, more modes will appear inside the cavity, which will again lead to  $B_1^+$  field inhomogeneity [13]. By designing a metamaterial liner inside the MRI bore, a complex and dispersive permittivity profile can be achieved, which makes it possible to propagate a wave inside the MRI bore at a frequency below the traditional cutoff [14], [15], [16]. This kind of propagation will achieve high field homogeneity for low-field MRI but will not apply at high-field (i.e., high RF frequency) MRI, at which frequency

Manuscript received 19 September 2023; revised 12 January 2024 and 1 March 2024; accepted 17 March 2024. Date of publication 1 April 2024; date of current version 27 May 2024. This work was supported by the Research Grants Council of the Hong Kong SAR, China, under Project CityU 21211619 and Project AoE/E-101/23-N. (Corresponding author: Alex M. H. Wong.)

Chen Xue and Guanglei Zhou are with the Department of Electrical Engineering, City University of Hong Kong, Hong Kong SAR, China (e-mail: chenxue7-c@my.cityu.edu.hk; guangzhou4-c@my.cityu.edu.hk).

Alex M. H. Wong is with the Department of Electrical Engineering, City University of Hong Kong, Hong Kong SAR, China, and also with the State Key Laboratory of Terahertz and Millimeter Waves, City University of Hong Kong, Hong Kong SAR, China (e-mail: alex.mh.wong@cityu.edu.hk).

Digital Object Identifier 10.1109/JERM.2024.3381333

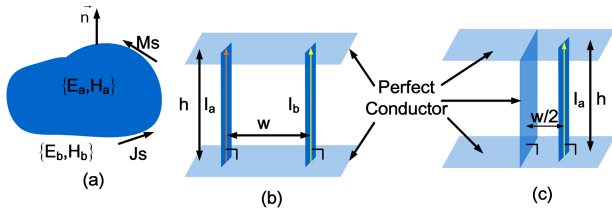


Fig. 1. (a) Diagram of the electromagnetic equivalence principle. (b) Huygens' source metasurface elements, where  $I_a$  and  $I_b$  are the currents run through the strips,  $h$  is parallel-plate separation,  $w$  is the distance between the currents,  $I_a$  and  $I_b$  are orthogonal to the parallel plates. (c) Simplified Huygens' source.

the MRI bore is above cut-off and may even feature multiple propagation modes (which in general have inhomogeneous field distribution).

In this paper, we propose a new method – the Huygens' cylinder – to generate a homogeneous RF  $B_1^+$  field inside an MRI bore. This method operates regardless of the electrical size of the bore and can hence be applied to HF as well as UHF MRI. The Huygens' cylinder generates a circularly polarized travelling plane wave with very high purity for both 3T and 7T MRI, which has better field homogeneity than even the fundamental mode of the TW-MRI method. By invoking the electromagnetic equivalence principle [17], [18], we gain large freedom on wave manipulation inside the MRI bore, which we utilize to generate a homogeneous  $B_1^+$  field therein. The proposed method can be used to generate very uniform RF illumination in whole body imaging and body part imaging. In our previous work [19], we show the concept and the unloaded 3T Huygens' simulation results briefly, however the realistic size of the Huygens' cylinder for fitting the clinical MRI bore is not considered and thorough analysis results are not reported. In this manuscript, we analyze the field in much more details. In the following sections, we introduce the simulation setup, compare the conventional bird-cage coils and the proposed Huygens' cylinders. The simulation results show that it can generate homogeneous magnetic field in both sagittal and axial cross section regardless of the size of the bore, so that there is great potential of Huygens' cylinder in HF or UHF MRI.

## II. METHOD

### A. Concept

We first overview the Huygens' cylinder. Fig. 1 illustrates the active Huygens' box, which is a physical implementation of the electromagnetic equivalence principle. We define the electromagnetic field inside and outside the enclosed region in Fig. 1(a) as  $\{\mathbf{E}_a, \mathbf{H}_a\}$  and  $\{\mathbf{E}_b, \mathbf{H}_b\}$ , respectively. The electromagnetic equivalence principle states that, by exciting a set of tangential surface electric and magnetic currents  $\{\mathbf{J}_s, \mathbf{M}_s\}$  on the boundary, one can generate a desired field  $\{\mathbf{E}_a, \mathbf{H}_a\}$  interior to the region independent from the exterior fields  $\{\mathbf{E}_b, \mathbf{H}_b\}$  [17], [18], [19], [20]. The required current can be calculated using:

$$\mathbf{J}_s = \hat{\mathbf{n}} \times (\mathbf{H}_b - \mathbf{H}_a)$$

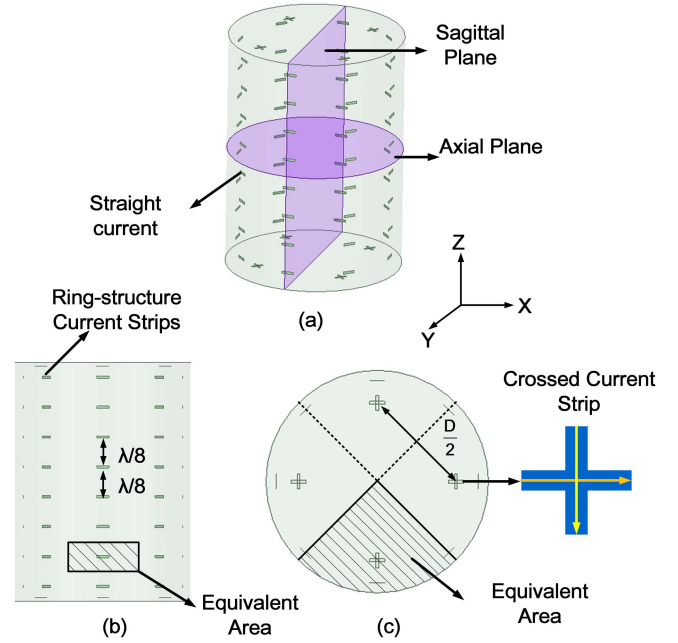


Fig. 2. Diagrams of the 7T Huygens' cylinder. (a) The perspective view; (b) The side and (c) top/bottom view. A similar setup with different source positions can be used for 3T MRI, where  $D$  is the diameter of the cylinder. Current on the straight and crossed strips corresponds to  $I_a$  in (c). Cylindrical bore corresponds to the perfect conductor in (b) and (c).

$$\mathbf{M}_s = -\hat{\mathbf{n}} \times (\mathbf{E}_b - \mathbf{E}_a) \quad (1)$$

where  $\hat{\mathbf{n}}$  represents the outward surface normal and  $\times$  indicates the cross product.

In our previous works [19], [20], [21], we have demonstrated the active Huygens' box concept, whereby one can freely synthesize electromagnetic waves inside an enclosed region by discretizing, then exciting, the electric and magnetic currents using the Huygens' source metasurface element shown in Fig. 1(b) and (c). In the simplified case of Fig. 1(c) the excitation current is [21]:

$$I = j \frac{s M_s}{\omega \mu_0 w} \quad (2)$$

where  $s$  is the separation between adjacent metasurface elements,  $w/2$  is the distance between metasurface element and the ground plane,  $M_s = \|\mathbf{M}_s\|$  is the complex magnitude of the magnetic surface current,  $\omega = 2\pi f$  is the angular frequency and  $\mu_0$  is the free space permeability. Using the active Huygens' box concept, we propose to line the cylindrical MRI bore with active metasurfaces which synthesize a right-hand circularly polarized (RHCP) plane wave (the  $B_1^+$  field) at the desired frequency. We call this setup the Huygens' cylinder. We achieve this by placing current strips, backed by a ground plane, along the interior of the MRI bore boundary as shown in Fig. 2. These current strips will implement the simplified Huygens' source shown in Fig. 1(c), with slight adjustments accounting for the slight curvature of the ground plane along the cylindrical MRI bore.

To calculate the required current excitations, we first express the desired RHCP wave as:

$$\begin{aligned} \mathbf{E} &= E_0 e^{j(kz + \varphi_0)} \hat{\mathbf{x}} + E_0 e^{j(kz + \varphi_0 - \pi/2)} \hat{\mathbf{y}} \\ \mathbf{H} &= \frac{1}{\eta_0} \hat{\mathbf{z}} \times \mathbf{E} \end{aligned} \quad (3)$$

where  $E_0$  is amplitude of the  $\mathbf{E}$  field,  $k$  is the wave number,  $\varphi_0$  is the initial phase and  $\eta_0 = \sqrt{\frac{\mu_0}{\epsilon_0}}$  is the intrinsic impedance of free space. Substituting these interior region fields (3) as  $\{\mathbf{E}_a, \mathbf{H}_a\}$  in (1), and requiring that no exterior fields be generated (i.e.,  $\{\mathbf{E}_b, \mathbf{H}_b\} = 0$ ), we use (1) to find the required magnetic current  $M_s$  at the locations of the current strips, then use (2) to find the required current  $I$  at each location (taken at the center of each current strip):

$$\vec{I} = \frac{sE_0}{\omega\mu_0 w} \cdot e^{j(kz + \varphi_0 + \frac{\pi}{2} - \theta)} \cdot (-\sin\theta \cdot \hat{\mathbf{x}} + \cos\theta \cdot \hat{\mathbf{y}}) \quad (4)$$

where  $\theta$  is the azimuthal location of the current strip in the loop. Exciting the current strips with the correct RF currents will synthesize the desired homogeneous  $B_1^+$  field inside the MRI bore.

Fig. 2 shows the placement of sources (i.e., the current strips), which form rings along the MRI bore. Each ring is made of eight current strips along the circumference of the bore. For 7T Huygens' cylinder, the rings are repeated every  $\lambda/8$  (125.8 mm) along the longitudinal direction. For 3T Huygens' cylinder, the rings are repeated every  $\lambda/16$  (146.8 mm) along the longitudinal direction. The current strips are 50.0 mm in length and 10.0 mm in width. Adjacent strips in the ring are separated by distance of 257.5 mm and 284.6 mm (center-to-center) for 7T case and 3T case, respectively. The Huygens' cylinder operates properly if the element separations are less than half-wavelength, as required by the Nyquist criterion. Nonetheless, a smaller separation allows the near field to settle in the very close vicinity of the boundary of the MRI bore, and hence achieve uniform field generation across a larger area of the bore [21]. We have found the above-mentioned separations to be sufficient for generating a homogeneous  $B_1^+$  field inside the MRI bore. Fig. 2(c) shows the inclusion of four cross-shaped current strips used to generate the required circularly polarized traveling wave. The vertical and horizontal components are excited in phase but are  $90^\circ$  phase-shifted to generate the  $B_1^+$  field stipulated in (3). The currents can be calculated using (1)–(3), but a multiplicative calibration factor needs to be applied to these end-plane currents, which accounts for (i) the difference in effective area as labelled in Fig. 2(b) and (c), (ii) the difference cause by the ground plane curvature along the MRI bore and (iii) the difference in coupling from the currents on the strip to the waveguide's propagation mode. While it is possible to obtain the calibration factor [22], [23] from analytical calculation, we have taken the accurate and straightforward approach of extracting this calibration factor from a full-wave simulation, in which we adjust this factor (in a post-processing procedure) until a homogeneous plane wave is achieved. Regarding the separation of sources at the ends of the MRI bore, again a half-wavelength spacing would be sufficient, and tighter/sparser spacing would improve/degrade

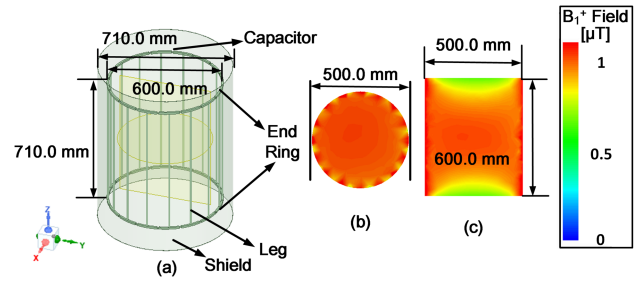


Fig. 3. (a) Diagram of the unloaded 3T Birdcage coil. (b) The complex magnitude of  $B_1^+$  field on the axial plane and (c) sagittal plane.

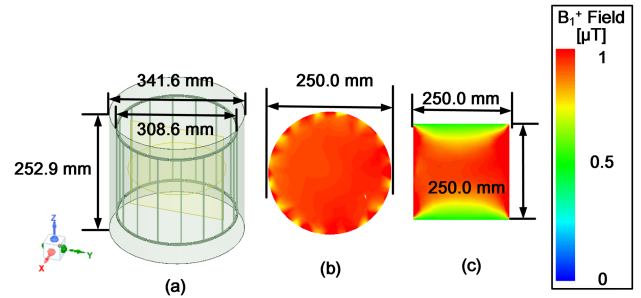


Fig. 4. (a) Diagram of the unloaded 7T Birdcage coil. (b) The complex magnitude of  $B_1^+$  field on the axial plane and (c) sagittal plane.

field uniformity close to the sources [21]. We have chosen a practical balance between the two and make the distance between crossed current strips  $\frac{D}{2}$ , where  $D$  is the diameter of the cylinder. In the 3T case,  $D = 0.33 \lambda$ . In the 7T case,  $D = 0.74 \lambda$ .

### B. Electromagnetic Simulation

The full-wave simulations in this paper are performed using the Ansys HFSS electromagnetic solver, which numerically solves Maxwell's equations using the finite element method (FEM). Given a known set of sources, materials and boundary information on the simulation domain, the FEM is invoked to solve Maxwell's equations to find the RF electric and magnetic fields within the simulation domain, which in this case is the MRI bore. Using this simulation tool, we compute the  $B_1^+$  field distribution for the Huygens' cylinder for both 3T and 7T MRI ( $f = 127.7$  MHz and  $f = 300.0$  MHz).

For comparison, we calculate the  $B_1^+$  field distribution of quadrature-driven high-pass birdcage coils for 3T and 7T MRI. Figs. 3(a) and 4(a) show the designed birdcage coils. The 3T coil features 16 rungs, a diameter of  $D = 600.0$  mm, a height of  $H = 710.0$  mm, and gap capacitances of  $C = 9.6$  pF. The coil is enclosed by a metallic shield, of diameter  $D_{\text{shield}} = 710.0$  mm. The 7T coil features 16 rungs, a diameter of  $D = 308.6$  mm, a height of  $H = 252.9$  mm, and gap capacitances of  $C = 5.4$  pF. The coil is enclosed by a metallic shield, of diameter  $D_{\text{shield}} = 341.6$  mm. For port matching, a 5 pF capacitor and a 0.2  $\mu\text{H}$  inductor are connected to the 50  $\Omega$  lumped port in series for 3T and 7T birdcage, respectively. After matching, we achieve a satisfactory  $S_{11}$  which is below  $-15$  dB for both 3T and 7T case.

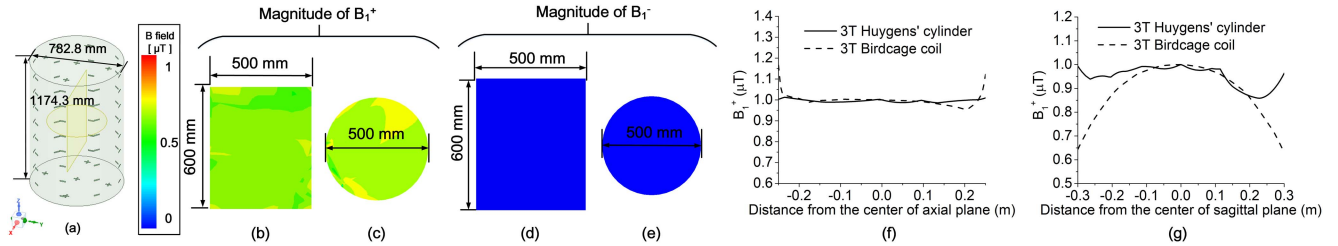


Fig. 5. (a) Diagram of the unloaded 3T Huygens' cylinder. The right-hand component of B field ( $B_1^+$ ) on the (b) sagittal plane and (c) axial plane. The left-hand component of B field ( $B_1^-$ ) on the (d) sagittal plane and (e) axial plane. (f) Comparison of normalized  $B_1^+$  field distribution on axial plane from 3T Huygens' cylinder and birdcage coil. (g) Comparison of normalized  $B_1^+$  field on sagittal plane from 3T Huygens' cylinder and birdcage coil.

For simulating loaded situations, we use cylindrical phantoms [24] with dielectric constant  $\epsilon_r = 58.1$  and conductivity  $\sigma = 0.54$  S/m, which are the average properties for human body, for both 3T and 7T Huygens' cylinders and the birdcage coils.

### III. RESULT

We report our simulation results for both the Huygens' cylinder and the birdcage coils. Our attention is on verifying the right-hand circularly polarized component  $B_R$  and the left-hand circularly polarized component  $B_L$  of the generated RF field. The generated field has high  $B_1^+$ -field homogeneity if it features uniform  $B_R$ . Further, efficiency would be optimal if only a  $B_R$  field (i.e., almost no  $B_L$  field) is generated. A highly homogeneous  $B_1^+$  field induces the same flip angle to all nuclei in the imaging plane, which means the decay signal collected by the receive coils will contain information on material properties, without degradation due to bright spots and dark spots.

#### A. Unloaded Simulation

We first examine the simulated RF field uniformity of the respective devices in an unloaded 3T MRI case. The coefficient of variation (CoV) of  $B_1^+$  field strength, defined as:

$$CoV = \frac{\sigma_B}{\mu_B}, \quad (5)$$

where  $\mu_B = (\sum_{i=1}^{i=N} |B_{1^+ i}|) / N$ , is the average value of  $B_1^+$  field strength in the observation set,  $N$  is the number of data in the observation set,  $\sigma_B = \sqrt{\sum_{i=1}^{i=N} (|B_{1^+ i}| - \mu_B)^2 / N}$ , is the standard deviation of  $B_1^+$  field strength in the observation set [25], [26]. We quantify the percentage-improvement of homogeneity as:

$$\%Homogeneity_{improvement} = CoV_{BC} - CoV_{HC}. \quad (6)$$

Figs. 3(a) and 5(a) gives the diagram of the 3T birdcage coil and the 3T Huygens' cylinder, respectively. The size of the Huygens' cylinder (1174.3 mm in length and 782.8 mm in diameter) is slightly larger than birdcage coil (710.0 mm in length and 710.0 mm in diameter). Figs. 3(b), (c) and 5(b), (c) show the  $B_1^+$  field strength of the two coils at the center axial plane and sagittal plane. From these sub-figures, we see that both schemes can generate a relatively uniform  $B_1^+$  field in the bore. Fig. 5(f) and (g) further compare the distribution of the normalized  $B_1^+$  field of the birdcage coil and the Huygens' cylinder over the

TABLE I  
COEFFICIENT OF VARIATION OF  $B_1^+$  FIELD MAGNITUDE OVER THE CERTAIN RANGES FOR 3T AND 7T MRI SYSTEM

3T MRI		
	BC	HC
Axial (500 mm)	2.7 %	0.6 %
Sagittal (600 mm)	12.1 %	4.5 %
7T MRI		
Axial (250 mm)	3.4 %	0.6 %
Axial (500 mm)	/	2.9 %
Sagittal (250 mm)	18.4 %	4.9 %
Sagittal (600 mm)	/	11.0 %

two planes. We can see that over the same region of interest 500 mm in diameter and 600 mm in height, the variation of the  $B_1^+$  field generated by Huygens' cylinder is smaller than the variation of the  $B_1^+$  field generated by birdcage coil. Both have a region where the  $B_1^+$ -field amplitude increases towards the edge of the MRI bore, due to the presence of a strong EM-field near the current. However, as this region should not contact the human body, it will not lead to non-uniform illumination in MR. Table I tabulates the coefficient of variation (CoV) of  $B_1^+$  field strength. In Table I, HC represents "Huygens' cylinder" while BC represents "birdcage coil". It shows that the 3T Huygens' cylinder achieves much better  $B_1^+$ -field uniformity on both axial and sagittal planes, by 2.1% and 7.6%, respectively, thus there is great advantage of field homogeneity from Huygens' cylinder.

We then present unloaded simulation results for the 7T MRI in Figs. 4, 6, and Table I. The length of the 7T Huygens' cylinder is set at one working wavelength, which is 1006.5 mm. Due to the structure limitation of birdcage coil, it cannot generate uniform  $B_1^+$  field over a large region of space. We therefore scale down the size of the 7T birdcage coil to 341.6 mm in diameter and 252.9 mm in height. A larger sized birdcage coil will have even worse  $B_1^+$  field homogeneity, because it will violate the electrostatic approximation. Figs. 4(b), (c) and 6(b), (c) show the  $B_1^+$  field strength of the birdcage coil and the Huygens' cylinder at the center axial and sagittal plane. The birdcage coil can generate a  $B_1^+$  field with homogeneity over 250 mm in diameter and 250 mm in length. The Huygens' cylinder can generate a uniform field over a much larger region with 500 mm in diameter and 700 mm in length. Fig. 6(f) and (g) compare the distribution of the normalized  $B_1^+$  field of birdcage coil and Huygens' cylinder over the axial and the sagittal plane. We

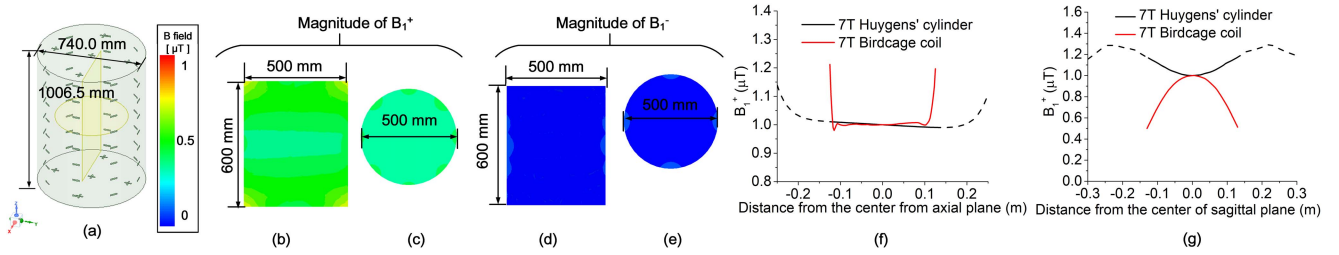


Fig. 6. (a) Diagram of the unloaded 7T Huygens' cylinder. The right-hand component of B field ( $B_1^+$ ) on the (b) sagittal plane and (c) axial plane. The left-hand component of B field ( $B_1^-$ ) on the (d) sagittal plane and (e) axial plane. (f) Comparison of normalized  $B_1^+$  field distribution on axial plane from 7T Huygens' cylinder and birdcage coil. (g) Comparison of normalized  $B_1^+$  field on sagittal plane from 7T Huygens' cylinder and birdcage coil.

TABLE II

COEFFICIENT OF VARIATION OF  $B_1^+$  MAGNITUDE VARIATION OVER AXIAL AND SAGITTAL LINES FOR 3T AND 7T MRI SYSTEMS LOADED WITH PHANTOMS

	3T MRI		7T MRI				
	BC	HC	BC	HC	BC	HC	
Axial (400 mm)	29.8%	30.3%	Axial (200 mm)	25.1%	31.7%	Axial (400 mm)	43.0%
Sagittal (500 mm)	22.0%	20.2%	Sagittal (250 mm)	41.8%	30.3%	Sagittal (500 mm)	37.2%

can see that over the same region of interest with 250 mm in diameter and 250 mm in height, the variation of the  $B_1^+$  field obtained from Huygens' cylinder is smaller than the  $B_1^+$  field generated by birdcage coil, by 2.8% in axial direction and 13.5% in sagittal direction. Moreover, Table I shows that a reasonably homogeneous  $B_1^+$  field can be achieved with the Huygens' cylinder at 7T over a 500 mm distance at the center axial plane and a 600 mm distance at the center sagittal plane. Such a large region of  $B_1^+$  field homogeneity cannot be achieved by the birdcage because of its limited size.

To investigate the homogeneity of the  $B_1^+$  field inside the cylinders, we compare the right-hand and left-hand circularly polarized components ( $B_1^+$  and  $B_1^-$ ) of the magnetic field within the 3T and 7T MRI bore at axial and sagittal planes, as shown in Figs. 5(b)–(e) and 6(b)–(e). It shows that for both the 3T and 7T Huygens' cylinders,  $B_1^-$  is very weak, while  $B_1^+$  is with a constant magnitude, which means that the fields generated inside the Huygens' cylinder are right-hand circularly polarized with very high mode purity.

### B. Loaded Simulation

We proceed to provide simulation results for loaded situations. For comparison, the source strengths are tuned such that the  $|B_1^+|$  at the center point is 1  $\mu$ T. The specific absorption rate (SAR), which is defined by:

$$SAR(\mathbf{r}) = \frac{\sigma(\mathbf{r}) |\mathbf{E}(\mathbf{r})|^2}{2\rho(\mathbf{r})}, \quad (7)$$

is used to measure the amount of radiation absorbed by human tissues. In (7),  $\mathbf{r}$  represents a location within the subject with conductivity  $\sigma(\mathbf{r})$ , density  $\rho(\mathbf{r})$ , and electric field amplitude  $|\mathbf{E}(\mathbf{r})|$ . In the following section, we compare  $SAR_{10g}$  and  $SAR_{average}$  in the phantoms obtained from the Huygens' cylinders and birdcage coils.

We first show the  $B_1^+$  distribution and SAR distribution for the loaded 3T case. The cylindrical phantom which is 400 mm

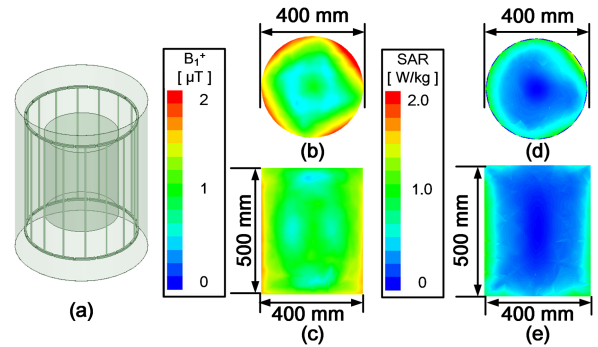


Fig. 7. (a) Diagram of the loaded 3T birdcage coil. The  $B_1^+$  field distribution obtained from 3T birdcage coil over the (b) axial and (c) sagittal plane. The SAR distribution obtained from 3T birdcage coil over the (d) axial and (e) sagittal plane.

in diameter and 500 mm in length is placed at the center of 3T birdcage coil and the 3T Huygens' cylinder, as shown in Figs. 7(a) and 8(a). Figs. 7(b), (c) and 8(b), (c) show the  $B_1^+$  distribution on the axial and sagittal plane from 3T birdcage coil and Huygens' cylinder. Reasonable  $B_1^+$  homogeneity is obtained from both coils. Table II shows the  $B_1^+$  CoV along the axial and sagittal planes for both coils. The CoV of  $B_1^+$  from the loaded 3T Huygens' cylinder is superior to the 3T birdcage coil in sagittal direction by 1.8% and slightly inferior to the 3T birdcage coil in axial direction by 0.5%, which means after the placement of the phantom, we still can expect slightly more homogeneous  $B_1^+$  field inside the phantom from 3T Huygens' cylinder. Figs. 7(d), (e) and 8(d), (e) show the local  $SAR_{10g}$  on the axial and sagittal planes from 3T birdcage coil and Huygens' cylinder. The maximum local  $SAR_{10g}$  and average SAR values are tabulated in Table III. We see that the SAR performance from 3T Huygens' cylinder has slightly higher SAR values than the 3T birdcage coil. Both coils satisfy the IEC SAR standard, which is 3.2 W/kg for head  $SAR_{average}$  and 10 W/kg for head  $SAR_{10g}$ .

TABLE III  
SAR VALUE FOR LOADED 3T AND 7T MRI

	Maximum local SAR <sub>10g</sub> (W/kg)		Average SAR(W/kg)	
	BC	HC	BC	HC
3T MRI	1.58	2.13	0.41	0.44
7T MRI (Case I)	0.43	1.04	0.18	0.25
7T MRI (Case II)	/	6.12	/	0.64

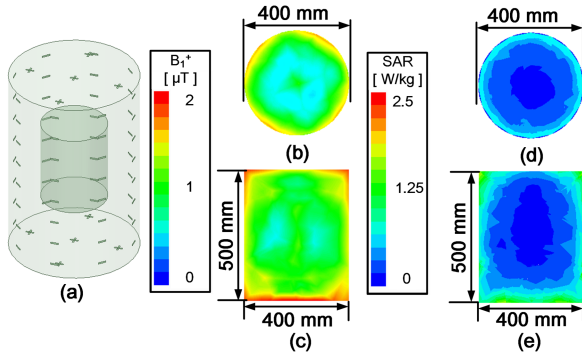


Fig. 8. (a) Diagram of the loaded 3T Huygens' cylinder. The  $B_1^+$  field distribution obtained from 3T Huygens' cylinder over the (b) axial and (c) sagittal plane. The SAR distribution obtained from 3T Huygens' cylinder over the (d) axial and (e) sagittal plane.

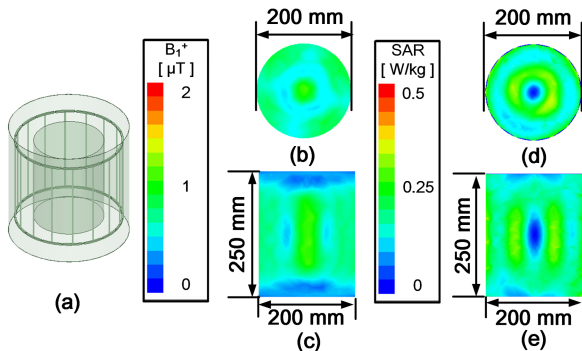


Fig. 9. (a) Diagram of the loaded 7T birdcage coil. The  $B_1^+$  field distribution obtained from 7T birdcage coil over the (b) axial and (c) sagittal plane. The SAR distribution obtained from 7T birdcage coil over the (d) axial and (e) sagittal plane.

Finally, we show the  $B_1^+$  distribution and SAR distribution for the loaded 7T cases. A smaller cylindrical phantom, 200 mm in diameter and 250 mm in length, is placed into the 7T birdcage coil and the 7T Huygens' cylinder, as shown in Fig. 9 and in Case I of Fig. 10. Figs. 9(b), (c) and 10(b), (c) show the  $B_1^+$  distribution on the axial and sagittal plane from 3T birdcage coil and Huygens' cylinder. Table II reports the  $B_1^+$  field CoV for both coils. From the table, we see that the  $B_1^+$  homogeneity from 7T Huygens' cylinder outperforms 7T birdcage coil by 11.5% on the sagittal plane, but the birdcage coil is more homogeneous than the Huygens' cylinder by 6.6% on the axial plane. While the 7T birdcage coil has size limitations due to its working mechanism, the Huygens' cylinder is free from such limitation. We place a larger phantom, which is 400 mm in diameter and 500 mm in height, inside the 7T Huygens' cylinder.

The simulation results are shown in Fig. 10(Case II). Case II of Fig. 10(g) and (h) show the  $B_1^+$  field distribution on the axial and sagittal plane respectively; the CoV values are tabulated in Table II. While the field variation worsens a bit compared to the small phantom case, we observe that a reasonable homogeneity can be maintained over a very large region.

Figs. 9(d), (e) and 10(d), (e), (i), (j), and Table III show the SAR distribution on the axial and sagittal planes for 7T birdcage coil and Huygens' cylinder. A slightly lower SAR is achieved from 7T birdcage coil in general. Notwithstanding, we show that the SAR produced by the Huygens' cylinder is comparable to that of the birdcage and satisfies the IEC safety requirement.

#### IV. DISCUSSION

In this paper, we apply the Huygens' approach to launch the sources for 3T and 7T MRI system. It is based on the electromagnetic equivalence principle, which is fundamentally different from previous RF excitation methodologies such as the birdcage or travelling wave MRI. This difference leads to unprecedented controllability on the fields within the MRI bore.

Our simulation results show that indeed the Huygens' cylinder superior  $B_1^+$  field uniformity and (in the 7T case) a similar uniformity but over a much larger region than possible with the birdcage coil. For unloaded 3T MRI, the Huygens' cylinder generates a more uniform field over 500 mm in the axial direction and 600 mm in the sagittal direction. The  $B_1^+$  CoV improvements over the two planes are 2.1% and 7.6% respectively, compared to the birdcage coil. A similar analysis for 7T MRI system shows that the Huygens' cylinder generates a homogeneous field over 500 mm in the axial direction and 600 mm in the sagittal direction. The  $B_1^+$  CoV is improved by 2.8% and 13.5% respectively in the axial and sagittal planes compared to a birdcage coil which is 341.6 mm in diameter and 252.9 mm in height. We note that in addition to achieving a large  $B_1^+$  homogeneity improvement, the size of the Huygens' cylinder is also much expanded to allow high-quality HF MR imaging for the human head and/or the torso. The loaded simulations results show that the presence of the phantom inside the coil somewhat degrades the  $B_1^+$  field homogeneity as would be expected. Nonetheless the Huygens' cylinder produces  $B_1^+$  field variations which are in some case better and in some cases comparable to those produced by birdcage coils. In the future, one can investigate whether further improvements to homogeneity can be achieved in loaded cases by including a generalized phantom in the initial current weight calculation, as currently (3) and (4) assume an unloaded region inside the coil.

Besides  $B_1^+$  field uniformity, SAR and SAR efficiency is also important for RF coils. The  $B_1^+$  field strength at the center of the coils is adjusted to  $1\mu\text{T}$  for both loaded 3T and 7T MRI.

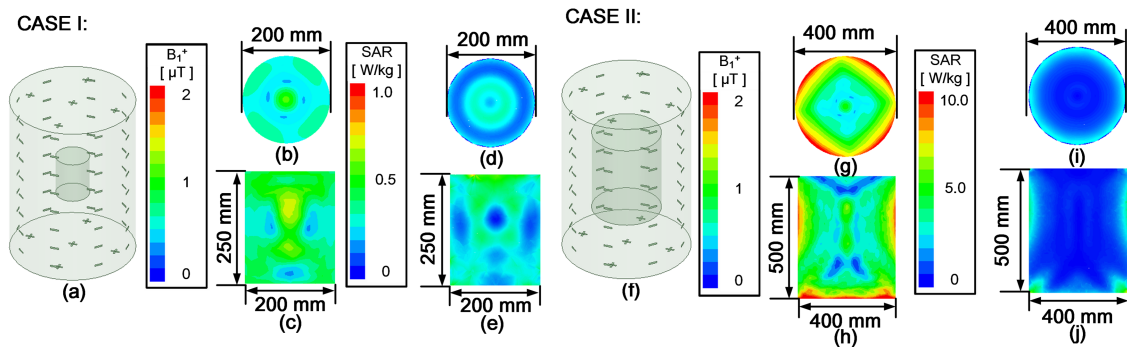


Fig. 10. (a) Diagram of the loaded 7T Huygens' cylinder. The  $B_1^+$  field distribution obtained from 7T Huygens' cylinder over the (b) axial and (c) sagittal plane. The SAR distribution obtained from 7T Huygens' cylinder over the (d) axial and (e) sagittal plane. (f) The diagram of the loaded 7T Huygens' cylinder. The  $B_1^+$  field distribution obtained from 7T Huygens' cylinder over the (g) axial and (h) sagittal plane. The SAR distribution obtained from 7T Huygens' cylinder over the (i) axial and (j) sagittal plane. (Fig. 10(a)–(e) are simulation results for CASE I: 7T Huygens' cylinder contained with cylindrical phantom which is 200 mm in diameter and 250 mm in height; Fig. 10(f)–(j) are simulation results for CASE II: 7T Huygens' cylinder contained with cylindrical phantom which is 400 mm in diameter and 500 mm in height.)

Under this field strength standard, find the SAR efficiencies to be 0.69 and 0.98 for 3T and 7T Huygens' cylinder, respectively, and 0.8 and 1.52 for 3T and 7T birdcage coil, respectively. In general, the birdcage coil achieves lower SAR values, and in turn, higher SAR efficiency because the electric field, which leads to power absorption, vanishes along the longitudinal axis (z-axis) of the coil while the magnetic field reaches a peak value. This is a hallmark of a standing wave pattern not shared by the Huygens' cylinder, which synthesizes the travelling wave where the electric field strength is, by and large, linearly proportional to the magnetic ( $B_1^+$ ) field strength. Since the Huygens' cylinder provides tremendous flexibility in modifying the electromagnetic waveform, it will be of interest to investigate whether it can generate a highly homogeneous  $B_1^+$  field along with a relatively low amplitude E field, which will increase the SAR efficiency. In any case, in all cases shown in this paper the Huygens' cylinder achieves SAR values which are within the IEC safety standard.

In addition, we note that the above calculation for efficiency for the Huygens cylinder represents a theoretical study only; practical problems, such as impedance matching, properly cycling and phasing the currents on the microstrip patches and power tuning between the current strips on the side and the two ends of the cylinder, need to be resolved. In a forthcoming work, we will investigate the practical, power-efficient design of the Huygens' cylinder using the concept of active series-fed metasurface [27].

## V. CONCLUSION

The Huygens' cylinder is proposed as a new methodology for RF ( $B_1^+$ ) field generation in MRI. Using this method, we have demonstrated the achievement of a highly homogeneous  $B_1^+$  field over an arbitrarily large region enclosed by the cylinder. The uniformity level of  $B_1^+$  field for 3T MRI is clearly improved by the Huygens' cylinder. Both the level of homogeneity and the region over which it is achieved much surpasses conventional methods for the 7T MRI system. After the placement of testing phantoms, for both 3T and 7T case, the Huygens' cylinder

outperforms the birdcage in terms of  $B_1^+$  variation over the sagittal plane, and their  $B_1^+$  variations over the axial plane are comparable. The average SAR of Huygens' cylinder and birdcage coil is comparable from both 3T and 7T case. However, the maximum SAR<sub>10g</sub> from birdcage coil is considerably lower than Huygens' cylinder.

Field homogeneity is crucial for the obtaining of high-quality MR images. The proposed Huygens' cylinder achieves superior homogeneity over an unprecedented region. Importantly, the reliance on electromagnetic equivalence allows the Huygens' cylinder to operate for different bore sizes and RF frequencies, making it applicable to 3T MRI, 7T MRI and beyond. These traits make the Huygens' cylinder very attractive candidate for consideration in future UHF MRI systems.

## REFERENCES

- [1] V. Taracila, L. S. Petropoulos, T. P. Eagan, and R. W. Brown, "Image uniformity improvement for birdcage-like volume coils at 400 MHz using multi-channel excitations," *Concepts Magn. Reson. Part B: Magn. Reson. Eng.: An Educ. J.*, vol. 29, no. 3, pp. 153–160, 2006, doi: [10.1002/cmr.b.20067](https://doi.org/10.1002/cmr.b.20067).
- [2] C. E. Hayes, W. A. Edelstein, J. F. Schenck, O. M. Mueller, and M. Eash, "An efficient, highly homogeneous radiofrequency coil for whole-body NMR imaging at 1.5 T," *J. Magn. Reson.*, vol. 63, no. 3, pp. 622–628, 1985, doi: [10.1016/0022-2364\(85\)90257-4](https://doi.org/10.1016/0022-2364(85)90257-4).
- [3] J. Tropp, "The theory of the bird-cage resonator," *J. Magn. Reson.*, vol. 82, no. 1, pp. 51–62, 1989, doi: [10.1016/0022-2364\(89\)90164-9](https://doi.org/10.1016/0022-2364(89)90164-9).
- [4] P. Roschmann, "Radiofrequency penetration and absorption in the human-body: limitations to high-field whole-body nuclear-magnetic-resonance imaging," *Med. Phys.*, vol. 14, no. 6, pp. 922–931, 1987, doi: [10.1118/1.595995](https://doi.org/10.1118/1.595995).
- [5] C. Wang et al., "A practical multinuclear transceiver volume coil for in vivo MRI/MRS at 7 T," *Magn. Reson. Imag.*, vol. 30, no. 1, pp. 78–84, 2012, doi: [10.1016/j.mri.2011.08.007](https://doi.org/10.1016/j.mri.2011.08.007).
- [6] N. A. Bock, B. J. Nieman, J. B. Bishop, and R. M. Henkelman, "In vivo multiple-mouse MRI at 7 Tesla," *Magn. Reson. Med.: An Official J. Int. Soc. Magn. Reson. Med.*, vol. 54, no. 5, pp. 1311–1316, 2005, doi: [10.1002/mrm.20683](https://doi.org/10.1002/mrm.20683).
- [7] D. C. Alsop, T. J. Connick, and G. Mizsei, "A spiral volume coil for improved RF field homogeneity at high static magnetic field strength," *Magn. Reson. Med.*, vol. 40, no. 1, pp. 49–54, 1998, doi: [10.1002/mrm.1910400107](https://doi.org/10.1002/mrm.1910400107).
- [8] C. Sung-Taek, S. Yoon-Mi, and C. Jong-Woon, "Analysis of endcap effect for MRI birdcage RF coil by FDTD method," *Invest. Magn. Reson. Imag.*, vol. 7, no. 2, pp. 137–143, 2003, doi: [10.1109/RFM.2018.8846521](https://doi.org/10.1109/RFM.2018.8846521).

- [9] M. A. Erturk, A. J. Raaijmakers, G. Adriany, K. Ugurbil, and G. J. Metzger, "A 16-channel combined loop-dipole transceiver array for 7 Tesla body MRI," *Magn. Reson. Med.*, vol. 77, no. 2, pp. 884–894, 2017, doi: [10.1109/DD.2015.7354836](https://doi.org/10.1109/DD.2015.7354836).
- [10] P. Heo et al., "A study on multiple array method of birdcage coils to improve the signal intensity and homogeneity in small-animal whole-body magnetic resonance imaging at 7 T," *Int. J. Imag. Syst. Technol.*, vol. 30, no. 1, pp. 31–44, 2020, doi: [10.1002/ima.22383](https://doi.org/10.1002/ima.22383).
- [11] B. Akin and A. C. Özen, "Microstrip array insert for head coils: Towards layer fMRI at high fields," in *Proc. ISMRM 27th Annu. Meeting Exhib.*, 2019, p. 0371, doi: [10.1002/9780470034590.emrstm1096](https://doi.org/10.1002/9780470034590.emrstm1096).
- [12] D. O. Brunner, N. De Zanche, J. Fröhlich, J. Paska, and K. P. Pruessmann, "Travelling-wave nuclear magnetic resonance," *Nature*, vol. 457, no. 7232, pp. 994–998, 2009, doi: [10.1038/nature07752](https://doi.org/10.1038/nature07752).
- [13] I. A. Elabyad, T. Herrmann, J. Bernarding, and A. Omar, "Combination of travelling wave approach and microstrip transceiver coil arrays for MRI at 7 T," in *Proc. IEEE MTT-S Int. Microw. Symp.*, 2011, pp. 1–4, doi: [10.1109/MWSYM.2011.5972859](https://doi.org/10.1109/MWSYM.2011.5972859).
- [14] J. G. Pollock and A. K. Iyer, "Below-cutoff propagation in metamaterial-lined circular waveguides," *IEEE Trans. Microw. Theory Techn.*, vol. 61, no. 9, pp. 3169–3178, Sep. 2013, doi: [10.1049/el:19660029](https://doi.org/10.1049/el:19660029).
- [15] A. M. Maunder, C. Barker, N. De Zanche, and A. K. Iyer, "Metamaterial liner for MRI excitation—Part 1: Theory, modeling and design," *IEEE Access*, vol. 10, pp. 41664–41677, Apr. 2022, doi: [10.1109/ACCESS.2022.3167432](https://doi.org/10.1109/ACCESS.2022.3167432).
- [16] A. Maunder, N. De Zanche, and A. K. Iyer, "Simulation comparison of birdcage coil and metamaterial liner for MRI at 3T and 4.7 T," in *Proc. 50th Eur. Microw. Conf.*, pp. 1067–1070, 2021, doi: [10.23919/EuMC48046.2021.9338226](https://doi.org/10.23919/EuMC48046.2021.9338226).
- [17] H. M. Macdonald, "The integration of the equations of propagation of electric waves," *Proc. London Math. Soc.*, vol. 2, no. 1, pp. 91–95, 1912, doi: [10.1098/rsta.1901.0013](https://doi.org/10.1098/rsta.1901.0013).
- [18] S. A. Schelkunoff, "Some equivalence theorems of electromagnetics and their application to radiation problems," *Bell Syst. Tech. J.*, vol. 15.1, pp. 92–112, 1936, doi: [10.1002/j.1538-7305.1936.tb00720.x](https://doi.org/10.1002/j.1538-7305.1936.tb00720.x).
- [19] C. Xue, G. G. L. Zhou, and A. M. H. Wong, "Improving homogeneity for MRI RF field at 3T using a Huygens' box," in *Proc. IEEE Int. Symp. Antennas Propag. North Amer. Radio Sci. Meeting*, 2020, pp. 915–916, doi: [10.1109/IEEECONF35879.2020.9329556](https://doi.org/10.1109/IEEECONF35879.2020.9329556).
- [20] A. M. H. Wong and G. V. Eleftheriades, "Active Huygens' box: Metasurface-enabled arbitrary electromagnetic wave generation inside a cavity," 2018, arXiv:1810.05998.
- [21] A. M. H. Wong and G. V. Eleftheriades, "Active Huygens' box: Arbitrary electromagnetic wave generation with an electronically controlled metasurface," *IEEE Trans. Antennas Propag.*, vol. 69, no. 3, pp. 1455–1468, Mar. 2020, doi: [10.1109/TAP.2020.3017438](https://doi.org/10.1109/TAP.2020.3017438).
- [22] G. V. Eleftheriades et al., "Some important properties of waveguide junction generalized scattering matrices in the context of the mode matching technique," *IEEE Trans. Microw. Theory Techn.*, vol. 42, no. 10, pp. 1896–1903, Oct. 1994, doi: [10.1109/22.320771](https://doi.org/10.1109/22.320771).
- [23] V. Zhurbenko, Ed., *Passive Microwave Components and Antennas*. Rijeka, Croatia: InTech, 2010, doi: [10.5772/226](https://doi.org/10.5772/226).
- [24] V. Panda et al., "Metamaterial zeroth-order resonator RF coil for human head: Preliminary design for 10.5 T MRI," *IEEE J. Electromagnetics, RF Microw. Med. Biol.*, vol. 3, no. 1, pp. 33–40, Mar. 2019, doi: [10.1109/JERM.2019.2893546](https://doi.org/10.1109/JERM.2019.2893546).
- [25] A. L. H. M. W. Van Lier et al., "Electrical properties tomography in the human brain at 1.5, 3, and 7 T: A comparison study," *Magn. Reson. Med.*, vol. 71, no. 1, pp. 354–363, 2014, doi: [10.1002/mrm.24637](https://doi.org/10.1002/mrm.24637).
- [26] B. S. Park et al., "RF safety evaluation of a breast tissue expander device for MRI: Numerical simulation and experiment," *IEEE Trans. Electromagn. Compat.*, vol. 59, no. 5, pp. 1390–1399, Oct. 2017, doi: [10.1109/TEMC.2017.2678201](https://doi.org/10.1109/TEMC.2017.2678201).
- [27] C. Xue and A. M. H. Wong, "A wide-angle series-fed active metasurface," in *Proc. IEEE Asia-Pacific Microw. Conf.*, 2020, pp. 267–269, doi: [10.1109/APMC47863.2020.9331551](https://doi.org/10.1109/APMC47863.2020.9331551).